Text and references accompanying Nevada Bureau of Mines and Geology Map 190

Surface Rupture Map of the 2020 M6.5 Monte Cristo Range Earthquake, Esmeralda and Mineral Counties, Nevada

by

Seth Dee[1], Rich D. Koehler[1], Austin J. Elliott[2], Alexandra E. Hatem[2], Alexandra J. Pickering[2], Ian Pierce[3], Gordon G. Seitz[4], Camille M. Collett[2], Timothy E. Dawson[4], Conni De Masi[5], Craig M. dePolo[1], Evan J. Hartshorn[6], Christopher M. Madugo[7], Charles C. Trexler[2], Danielle M. Verdugo[8], Steven G. Wesnousky[9], and Judith Zachariasen[4]

[1]Nevada Bureau of Mines and Geology, University of Nevada, Reno
[2]U.S. Geological Survey; [3]University of Oxford; [4]California Geological Survey; [5]University of Nevada, Reno, Nevada Bureau of Mines and Geology, Reno, NV; [6]Desert Research Institute; [7]Pacific Gas and Electric Company; [8]University of California, Los Angeles; [9]Nevada Seismological Laboratory, University of Nevada, Reno

2021

ABSTRACT

The 15 May 2020, M6.5 Monte Cristo Range earthquake produced surface rupture distributed across a 28-km-long zone along the eastward projection of the Candelaria fault in the Mina deflection of the central Walker Lane, Nevada. Post-event field surveys mapped surface ruptures and measured displacements, which reached up to ~20 cm of oblique slip. Additional detailed mapping was completed using centimeter-resolution orthomosaics generated from Uncrewed Aerial Vehicle surveys. The rupture observations and displacement data are compiled into this 1:14,000-scale map, data tables, and accompanying digital dataset. The rupture consists of two distinct deformational domains roughly separated by U.S. Highway 95: ENE-trending ruptures with normal and left-oblique displacements in the western domain, and N- to NNE-trending ruptures with normal and right-oblique displacement in the eastern domain. The complex pattern of surface rupture is consistent with the projections of mapped bedrock and Quaternary faults in the area and illustrates the kinematics of slip partitioning at the junction of variably oriented structures in the shallow subsurface.

INTRODUCTION

The 15 May 2020, M6.5 Monte Cristo Range earthquake was the largest earthquake in Nevada in over 66 years and occurred in a sparsely populated area of western Nevada about 74 km southeast of the town of Hawthorne. The epicenter, located at 38.1626°N, 117.8695°W, was in the easternmost part of the Mina deflection, a tectonic domain within the central Walker Lane characterized by subparallel, east- and northeast-striking left-lateral and left-oblique normal faults (Wesnousky, 2005; Stewart, 1988; fig. 1). The aftershock seismicity extends across a ~30 km long, east-west oriented zone along the eastward projection of the Candelaria fault (Bormann et al., 2021; Ruhl et al., 2021; fig. 1). Ruhl et al. (2021) infer that the shallow aftershock sequence highlights a fault fracture mesh of complex, variably oriented structures that align with left-lateral, right-lateral, and normal mechanism nodal planes.

Shaking was widely felt throughout eastern and central California, across the entire state of Nevada, including Reno and Las Vegas, and as far east as Salt Lake City, Utah. Due to the remote location of the event, damage was minimal, with the costliest impact being settlement cracks across U.S. Highway 95 that resulted in temporary closure of the road (fig. 2). A multi-institution collaborative effort was initiated the day of the event to assess the distribution and style of surface deformation. The field response included the detailed mapping of a complex and broadly distributed surface rupture as well as the collection of coseismic surface offset data.

The surface ruptures are depicted in map sheets 1 and 2 as well as figure 3, and the offset data are presented in table 1. This report describes the earthquake setting, data collection and compilation methodology, and a synopsis of the character and style of the rupture. This map and report are a companion publication to Koehler et al. (2021), which contains a more detailed evaluation of the pattern and style of displacement, a comparison of the rupture mapping to

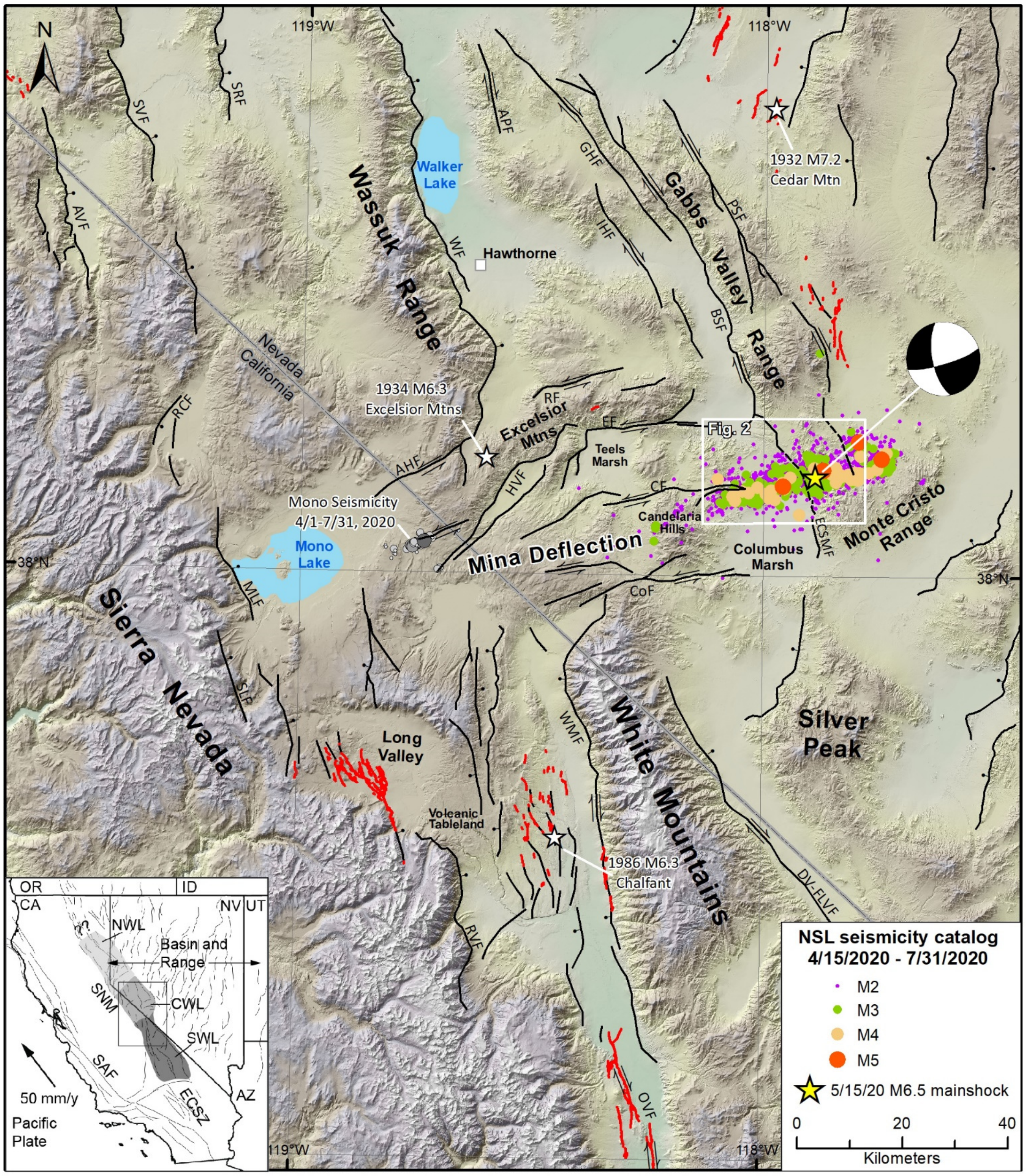

Figure 1. Tectonic setting of the Walker Lane and Basin and Range province in the western United States. The Walker Lane is shown as a shaded belt on the inset map, including the southern Walker Lane (SWL, dark gray), central Walker Lane (CWL, medium gray), and northern Walker Lane (NWL, light gray). Inset: San Andreas fault (SAF); Sierra Nevada microplate (SNM); eastern California shear zone (ECSZ). Main: Shaded relief map showing major faults in the region of the 2020 M6.5 Monte Cristo Range earthquake. Faults modified from Wesnousky (2005), Faulds and Henry (2008), and DeLano et al. (2019). Seismicity data from Nevada Seismological Lab (NSL) catalog (see Data Resources). Focal mechanism from the U.S. Geological Survey. White stars indicate historical earthquake epicenters as labeled and red lines indicate historical surface ruptures. Major faults of the Mina deflection are Anchorite Hills fault (AHF); Rattlesnake fault (RF); Huntoon Valley fault (HVF); Excelsior fault (EF); Candelaria fault (CF); and Coaldale fault (CoF). Other regional faults (black lines) include Agai Pah fault (APF); Antelope Valley fault (AVF); Benton Spring fault (BSF); Death Valley–Fish Lake Valley fault system (DV-FLVF); Gumdrop Hills fault (GHF); Eastern Columbus Salt Marsh fault (ECSMF), Indian Head fault (IHF); Mono Lake fault (MLF); Owens Valley fault (OVF); Petrified Spring fault (PSF); Robinson Creek fault (RCF); Round Valley fault (RVF); Silver Lake fault (SLF); Smith Valley fault (SVF); Singatse Range fault (SRF); Wassuk fault (WF); White Mountain fault (WMF).

geodetic and seismologic observations, and a discussion of the role of the earthquake in accommodating crustal strain in the Walker Lane. The complete rupture map geospatial data are available for download from the NBMG website [http://nbmg.unr.edu/Geohazards/Earthquakes/MonteCristoRangeEQData.html].

REGIONAL SETTING

The Monte Cristo Range earthquake surface rupture occurred partly along the Candelaria fault in the central Walker Lane in a region known as the Mina deflection (fig. 1). The central Walker Lane is part of the larger transtensional Walker Lane system (Stewart, 1988) that extends from the eastern California Shear Zone to the Modoc Plateau along the eastern side of the Sierra Nevada and accommodates ~20–25% of Pacific–North America relative shear (Pierce et al., 2021; Lifton et al., 2013; Hammond and Thatcher, 2007; Dixon et al., 2000; Bennett et al., 1999). The Mina deflection is characterized by a series of east- to northeast-striking left-lateral and left-oblique normal faults that form a right step between north-northwest-striking right-lateral and right-oblique normal faults to the southwest and northeast (Faulds and Henry, 2008; Wesnousky, 2005; Oldow et al., 1994; dePolo et al., 1993; Stewart, 1988). Southwest of the Mina deflection, right-lateral and right-oblique normal slip is accommodated along a series of north-northwest striking faults distributed between the Sierra Nevada range front and Silver Peak, including the Owens Valley fault and the Death Valley–Fish Lake Valley fault system (fig. 1). The ~100-km-long strike-slip Owens Valley fault was the source of the 1872 M7.8–7.9 Owens Valley fault earthquake, which produced lateral displacements up to 6 m (Bacon and Pezzopane, 2007; Haddon, et al., 2016; Beanland and Clark, 1994). At its northern end, slip along the Owens Valley fault is partitioned into oblique-normal deformation accommodated along the Round Valley fault (Sierra Nevada range front), the White Mountain fault, and a series of faults within the Volcanic Tableland (DeLano et al., 2019; Nagorsen-Rinke et al., 2013). Northeast of the Mina deflection, right-lateral shear is accommodated on a series of parallel northwest-striking faults that extend along the east and west side of the Gabbs Valley Range (fig. 1). These faults include from west to east the Indian Head, Gumdrop Hills, Benton Spring, and Petrified Spring faults (Lee et al., 2020). The 1932 Mw7.2 Cedar Mountain earthquake occurred to the east of these faults and was associated with right-lateral and normal displacements widely distributed along the 75 km length of the rupture (Bell et al., 1999).

Wesnousky (2005) inferred that the transfer of right-lateral slip across the Mina deflection is accommodated by clockwise rotation of crustal blocks bounded by east-striking left-lateral faults. The basins at the ends of the left-lateral faults in the Mina deflection are the result of extensional

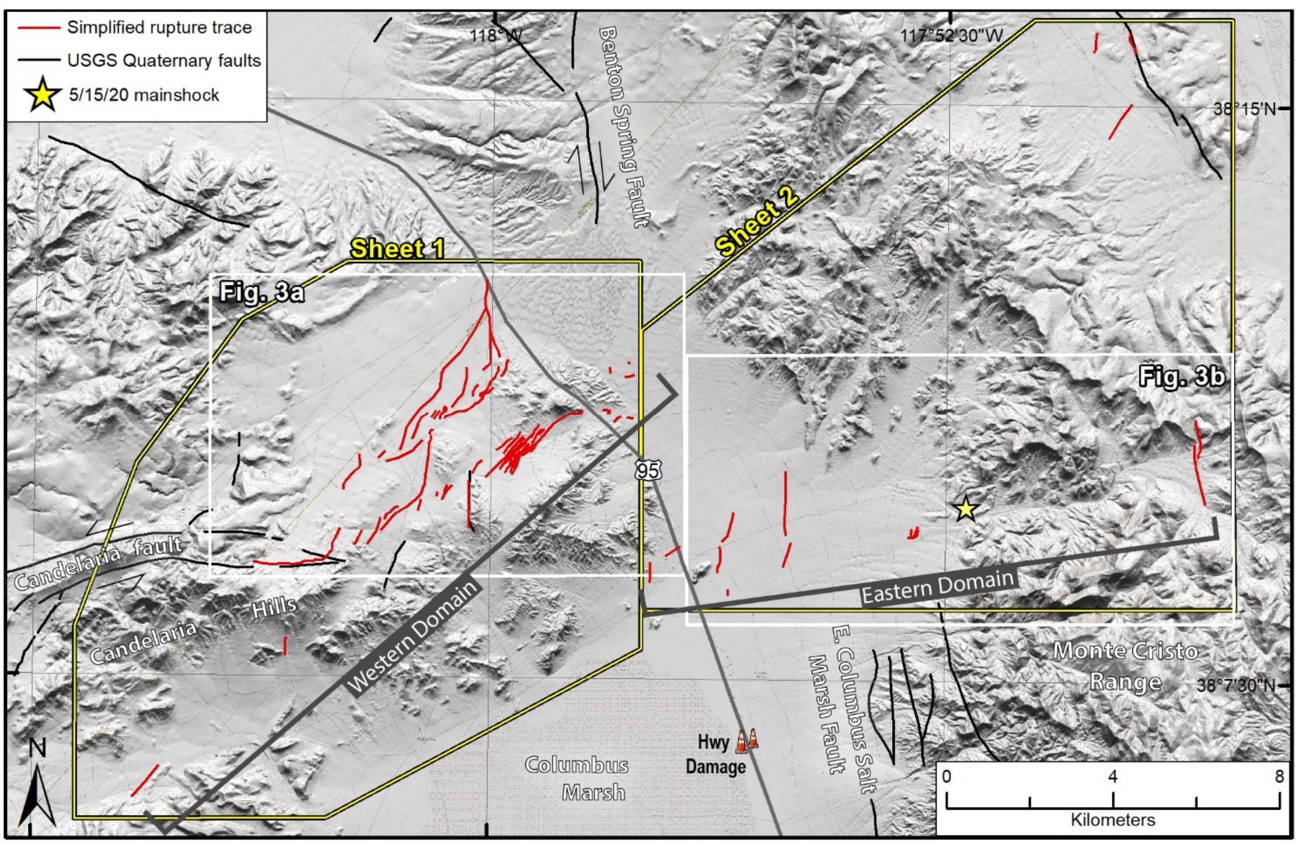

Figure 2. Surface rupture mapping from the M6.5 Monte Cristo Range earthquake showing mainshock epicenter, the eastern and western rupture domains, location of damage to U.S. Highway 95, and nearby mapped Quaternary faults (black lines; U.S. Geological Survey, 2006).

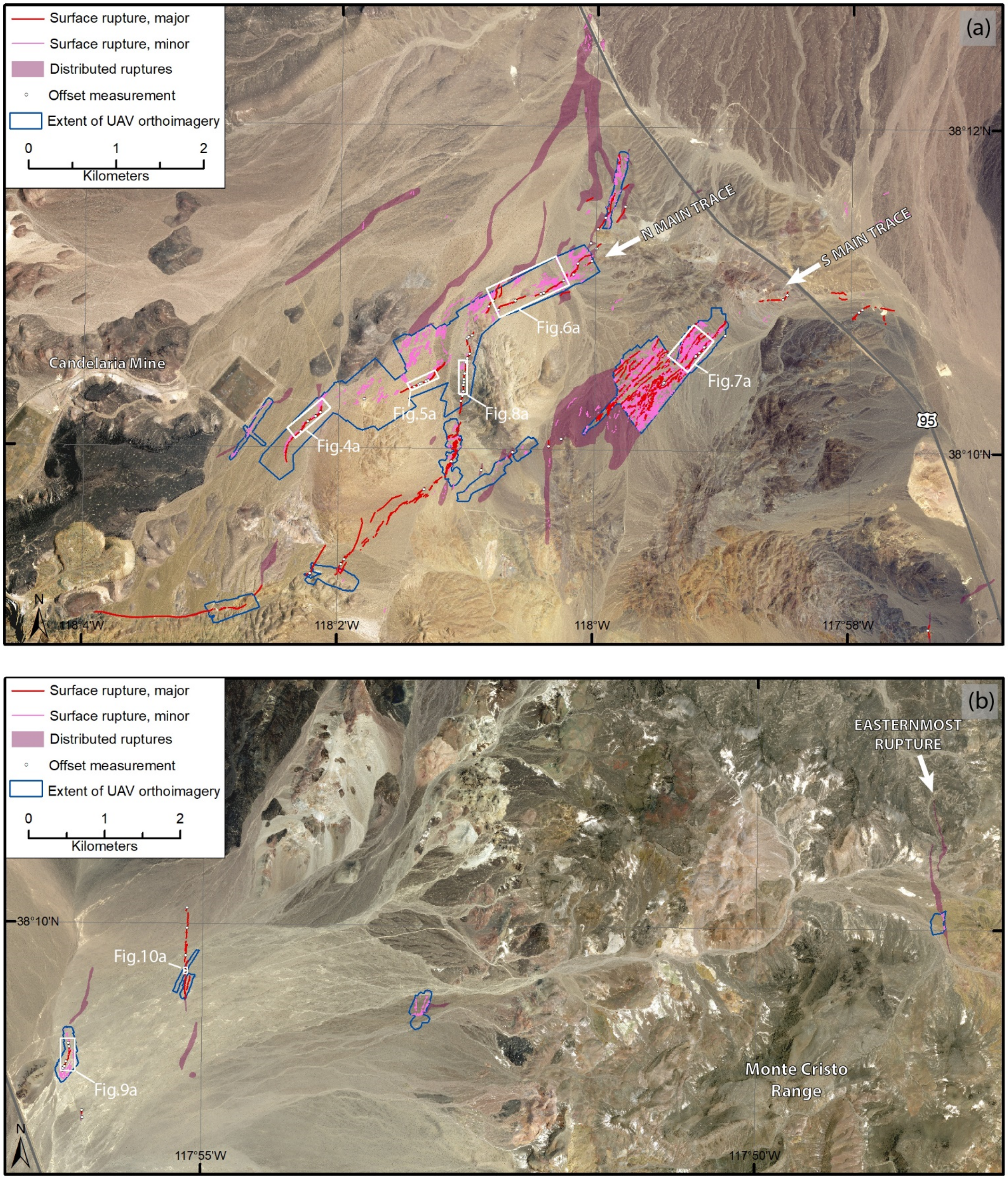

Figure 3. a) Surface rupture mapping in the main rupture zone of the western domain showing the north and south main traces. b) Surface rupture mapping in the main rupture zone of the eastern domain. Blue lines show the extent of orthomosaic and detailed rupture mapping. Rupture map includes main rupture traces (red lines), traces of fractures (pink lines), zones of distributed fractures in areas without detailed fracture mapping (purple polygons), and locations of displacement measurements.

accommodation adjacent to the rotating blocks. In this model, clockwise rotation of a block bound by the Candelaria fault to the north and Coaldale fault to the south resulted in the formation of the Columbus Salt Marsh basin (fig. 1). This model is consistent with paleomagnetic data showing 5°–60° of post-Miocene clockwise rotation of crustal blocks in the Mina deflection (Petronis et al., 2009), kinematic models using late-Cenozoic slip rates (DeLano et al., 2019; Nagorsen-Rinke et al., 2013), and rotation rates of 1–4°/Myr measured in geodetic block modeling (Bormann et al., 2016).

The Monte Cristo Range earthquake occurred within a spatial gap between major historical surface rupturing earthquakes to the northeast and south (fig. 1), specifically the 1932 Cedar Mountain (Bell et al., 1999) and the 1872 Owens Valley events (Beanland and Clark, 1994). While seismicity within the Mina deflection is generally diffuse, earthquake clusters with left-lateral focal mechanisms are relatively common (Ryall and Priestly, 1975), including events in 1980 and 1990 along the Coaldale and Huntoon Valley faults, respectively (dePolo et al., 1993). An east-west striking swarm of small to moderate earthquakes occurred just east of Mono Lake about a month before the Monte Cristo Range earthquake (fig. 1). The largest previously recorded earthquake within the Mina deflection, the 1934 M6.3 Excelsior Mountains earthquake, occurred in the vicinity of the Excelsior fault, approximately 20 km northwest of the Monte Cristo Range earthquake surface rupture (Callaghan and Gianella, 1935).

DATA COLLECTION

The geologic field assessment team included over 20 scientists from the Nevada Bureau of Mines and Geology (NBMG), California Geological Survey (CGS), U.S. Geological Survey (USGS), and several other organizations. Field surveys were conducted over a two-week period beginning on the day of the earthquake. Rapidly processed Interferometric Synthetic Aperture Radar (InSAR) data provided by the U.S. Geological Survey, the Jet Propulsion Laboratory (JPL), and other colleagues to field personnel in near real-time proved to be an invaluable resource for guiding the field mapping and locating the most continuous surface ruptures (Elliott et al., 2020). A rainstorm during the field response (May 19th, 2020) resulted in overland sheet flow causing the filling of cm-scale open cracks with sediment, and degradation of some subtle piercing points, highlighting the importance of rapid documentation of fragile geomorphic features associated with surface rupture.

Mapping teams used multiple data-collection technologies including hand-held GPS receivers, survey grade GPS receivers (Trimble GEO7X), and GPS-enabled smart phones and tablets (Apple iPads and iPhones). Data collected on smart phones and tablets were recorded using a variety of software applications (e.g. ESRI ArcGIS Collector; Avenza Maps; Touch GIS; MotionX GPS). Mapping methods included walking ruptures and recording locations with GPS waypoints, GPS tracks, and Geo7X survey tracks. The field teams recorded observations on the location, orientation, continuity, and patterns of surface ruptures, and where available, the amount and sense of coseismic surface offset. These data formed the basis for parts of the rupture mapping depicted in sheets 1 and 2.

Coseismic surface offsets were quantified by tape measurements at over 100 locations, and those offset measurements are presented in table 1. In general, centimeter-scale offsets were preserved in loosely consolidated deposits, within alluvial fan and pediment surfaces and the subtle margins of ephemeral stream channels, erosional rills and gullies. The data include location, sense of motion, amount of lateral and vertical offset, and field notes. The uncertainty in offset measurements of individual features is shown as a range in table 1 as well as on the sheets and figures.

Low altitude aerial imagery was collected using Uncrewed Aerial Vehicles (UAV, or drones) across areas of the most continuous surface ruptures. Sixteen UAV surveys were performed between May 16th and June 7th, 2020 covering a total of 3.7 km^2 of the rupture. Images were collected using a DJI Phantom 4 Pro and a DJI Phantom 3+. These images were processed with structure-from-motion (SfM) photogrammetric software to develop orthomosaics with resolutions ranging from 0.7–2.0 cm/pixel. Some, but not all of these SfM models were corrected using ground control points (GCPs) collected with survey-grade GPS systems. Those that were not referenced with GCPs relied on the on-board GPS in the UAV for spatial referencing. Absolute uncertainties therefore vary from <1 m for the models collected with GCPs to as much as 10 m for those without. However, orthomosaics are internally geometrically consistent and accurate. Subsequent to the field effort, the orthomosaics were used to map surface ruptures at large scales (<1:100), complementing field observations and illustrating the complexity of the rupture.

DATA COMPILATION AND RUPTURE MAP

Observations collected by the field assessment team were compiled by NBMG and formed the basis for much of the rupture mapping depicted in sheets 1 and 2. The UAV orthomosaics were important supplements to the field observations and allowed parts of the complex rupture to be depicted in much greater detail than would have been practical using ground-based data-collection methods. In some places duplicate, overlapping traces required reconciliation of the various line types. In these instances, lines digitized on orthomosaics with clear, high-resolution imagery were favored over lines collected by other methods. In areas lacking high-quality UAV imagery the linework from the GEO7X GPS was favored, followed by traces walked with tablet and phone track logs, and the least favored were lines interpolated between waypoints.

Each line feature in the compiled mapping was classified to reflect the deformational character of the feature. "Surface rupture, major" designates linear, relatively continuous cracks or fractures with locally measurable offset of surficial deposits or geomorphic features. "Surface rupture, minor" designates relatively discontinuous cracks or fractures (<1 to 10s of meters long) with offsets too small to be reliably measured (<~1cm). Both major and minor surface ruptures are inferred to be largely tectonic in origin (i.e., related to co-seismic fault slip and related bulk deformation in the shallow crust) because of having orientations and kinematics that are consistent with both the pattern of aftershock seismicity (Ruhl et al., 2021) and previously mapped faults in the area (USGS, 2006; Dohrenwend, 1982; Stewart et al., 1994). Commonly, minor surface ruptures are distributed cracks or dilational fractures, the origin of which may be attributable to either distributed fault rupture or earthquake-induced near-surface stress changes.

In many cases the distinction between major and minor ruptures was gradational, and thus categorization was subjective, relying on the judgement of team members who mapped particular rupture sections. While offsets on individual minor rupture traces were not measurable, collectively the zones of deformation may sum to significant displacement that would only be reliably measurable through differential remote sensing. In some cases, collections of short, low-offset cracks were arranged in close en échelon or semi-continuous geometries suggestive of a more significant throughgoing shear zone and were thus grouped together and classed as "major". The distinction between the two categories is presented to highlight structural coherency within the broadly distributed surface faulting.

"Secondary" features are confidently interpreted to have been produced by ground-shaking effects rather than tectonic deformation (e.g., mass wasting, liquefaction). "Ambiguous" lines are defined as linear features identified in the orthomosaics with low confidence that they originated during the earthquake. For legibility on the map sheets and figures, only "Surface rupture, major" and "Surface Rupture, minor" lines are shown; the complete set of lines is included in the digital database. Line classifications used in this map publication differ from those shown in Koehler et al. (2021); in that publication, "Surface rupture, major" is classified as "Main rupture" and "Surface rupture, minor" as "Fracture", reflecting the difference in whether offset was specifically measurable.

Given the highly distributed nature of the surface rupture, not all of the deformation could be mapped in full detail. Areas with field observations of distributed coseismic deformation, but where individual rupture traces were not surveyed and UAV orthomosaics were not collected, are shown on the map as polygons, reflecting observed zones of concentrated surface deformation (purple "Distributed ruptures" polygons on sheets 1 and 2; figs. 2 and 3). Similarly, rupture orientation measurements where ruptures were observed and measured but could not practically be mapped in detail are shown on the map with a linear symbol rotated to the orientation of the measured azimuth (sheets 1 and 2). Surface ruptures, offset measurements, zones of distributed minor surface rupture, rupture orientations, and the footprints of the orthomosaics are shown on sheets 1 and 2 at a scale of 1:14,000. The geospatial data shown in the rupture map are available to download at the NBMG website [http://nbmg.unr.edu/Geohazards/Earthquakes/MonteCristoRangeEQData.html]. The geospatial data include additional line and point data that were omitted from the map publication for visual clarity. A summary of the rupture map features and the data included in the geospatial datasets is shown on table 2.

PATTERN AND STYLE OF SURFACE RUPTURE

The surface ruptures were broadly distributed between the Candelaria Hills in the west and the Monte Cristo Range in the east and define an east-northeast trending zone 28 km long and locally up to 2.5–5 km wide (sheets 1 and 2; figs. 2 and 3). Two distinct domains of surface rupture in terms of style and orientation of displacements were observed, roughly separated by U.S. Highway 95, and informally named the western and eastern rupture domains (sheets 1 and 2 respectively; figure 2). Below we briefly summarize the general characteristics of the ruptures in each domain. Details of specific rupture areas are illustrated in maps, orthomosaics, and field photographs in figures 4–10. Additional details on the orientation, style, and distribution of ruptures within each domain are contained in Koehler et al. (2021).

Western Rupture Domain

In the western rupture domain, surface ruptures occurred along the northwestern flank of the Candelaria Hills within a broad zone of east-northeast-striking sinistral-oblique and north-northeast-striking extensional faults that extend for about 10 km from the eastern termination of the east-striking Candelaria fault near the Candelaria Mine to U.S. Highway 95 (sheet 1; fig. 3a). The observed surface ruptures coincide with the mapped trace of the Candelaria fault for a distance of ~2 km and continue northeast to within 3 km of the mapped trace of the Benton Spring fault (fig. 2; USGS, 2006). The ruptures extend across low bedrock hills, pediments, alluvial fans, and active washes. The ruptures commonly traverse geomorphic surfaces that lack clear evidence of recent Quaternary deformation (e.g., figs. 4 and 5); though in several locations, ruptures occur along pre-existing scarps and at the base of bedrock hills (e.g., fig. 6).

The western domain includes two subparallel traces (northern and southern) that strike between 040°–070° (fig. 3a). The two main traces are characterized by semi-continuous ruptures with measurable offsets fringed by zones of subparallel dilational cracks (pink lines and purple polygons in sheet 1 and figure 3a) that are open one to several centimeters and exhibit both sinuous and sawtooth edges. Sinistral-oblique ruptures commonly have overlapping right-stepping en échelon surface breaks, which are locally connected by 5–10 cm high push-up mounds and moletracks (fig. 5). The width of distributed deformation along the northern trace is about 500 m wide in the west and broadens to >2 km to the northeast. The southern main trace is about 20 m wide in the west, where it parallels the mapped trace of the Candelaria fault. The rupture expands eastward reaching a maximum width of 800 m in a zone of exceptionally distributed deformation in alluvial-fan deposits (fig. 7).

Measured left-lateral surface offsets range from 1–20 cm and 3–10 cm along the northern and southern main traces, respectively. Vertical offsets range from 1–10 cm along the northern main trace and are consistently down-to-the-northwest, whereas deformation across the zones of distributed ruptures along the southern main trace were comprised of primarily cm-scale dilations.

North-northeast-striking ruptures (5°–30°) splay off both the southern and northern main northeast-striking traces, extend for lengths of 0.5 to 1.8 km, and are associated with rupture zones between 10 and 100 m wide (sheet 1; figs. 3a and 8). These ruptures generally have down-to-the-west vertical separations that range from 1–5 cm, and locally exhibit left-stepping en échelon patterns.

Eastern Rupture Domain

Surface ruptures in the eastern rupture domain are distributed across a 14-km-wide area between U.S. Highway 95 and the Monte Cristo Range (sheet 2; figs. 2 and 3b). These rupture zones extend for lengths of 250 m to over 2 km and are predominantly characterized by north- to north-northeast-striking (350°–30°) extensional to oblique right-lateral ruptures. Individual ruptures are expressed as sinuous, anastomosing, and left-stepping extensional features that range in length from a few to several tens of meters (fig. 9). Extensional openings across individual cracks are typically 0.5–3 cm. Vertical separations are both down-to-the-east and -west and range from 2 to 5 cm. Right-lateral offsets were observed in several locations (max 11 cm) consistent with the left stepping en échelon pattern of individual traces (fig. 10).

Although ruptures in the eastern domain lack Quaternary geomorphic evidence of previous fault rupture, they occurred along projections of previously mapped faults; including the Quaternary Benton Spring, Columbus Salt Marsh, and Petrified Spring faults and a west dipping bedrock normal fault with 10s of meters of down-to-the-west displacement in the eastern Monte Cristo Range (USGS, 2006; Stewart, et al., 1994) (figs. 1 and 2).

SUMMARY

The Monte Cristo Range earthquake was the largest in Nevada in 66 years. A multi-institution field team mobilized to the epicentral area to document the distribution and style of surface rupture. The compiled earthquake rupture mapping is depicted in sheets 1 and 2. The earthquake involved simultaneous rupture and partitioning of slip into sinistral-oblique normal and dextral-oblique normal components across a 28-km-long network of faults that form a kinematic link between orthogonal regional faults.

In the western domain of the rupture, sinistral-oblique slip along northeast-striking faults and normal right-oblique slip along north-northeast-striking faults splay off the east-striking Candelaria fault and project for about 10 km eastward towards the northwest-striking right-lateral Benton Spring fault (fig. 2). The maximum observed left-lateral offsets are 20 cm and 10 cm along the northern and southern main traces, respectively, suggesting that the total maximum left-lateral slip was as much as 30 cm. However, the majority of individual measured offsets were less than 5 cm. Vertical offsets in the western domain were predominantly down-to-the-northwest and typically several centimeters (max 10.5 cm). In the eastern domain, normal and right-oblique slip on north-striking faults occurred along-strike of the Benton Spring, Petrified Spring, and Eastern Columbus Salt Marsh faults, as well as older mapped bedrock normal faults (fig. 2). Offsets here range between 2–5.5 cm (vertical) and 3–11 cm (right-lateral). Appreciable left-lateral slip was not observed along the eastern domain of the rupture. Thus, the zone of left-lateral slip was confined to the western domain of the rupture, representing approximately 36% of the 28-km-long zone of surface ruptures. The mainshock epicenter, which has an ENE-oriented left-lateral focal plane, is located in the eastern domain over 11 km east of the closest measurable left-lateral offset. Many of the major surface ruptures were also associated with broad zones of dilational cracks with individual openings typically from 1 to 3 cm.

The Monte Cristo Range earthquake surface rupture demonstrates the complex pattern of coseismic deformation associated with slip involving a network of faults within a Walker Lane displacement transfer zone (e.g. Oldow et al., 1994). Integration of the surface rupture characteristics (Koehler et al., 2021) with geodetic observations (Hammond et al., 2020) and aftershock seismicity (Ruhl et al., 2021) provides a three-dimensional perspective of coseismic strain from the earthquake.

ACKNOWLEDGMENTS

We are grateful for communication and dissemination of rapidly processed InSAR data during the field survey (U.S. Geological Survey: Ryan Gold, Rich Briggs, Stephen DeLong, Charles Wicks, and William Barnhart; Jet Propulsion Laboratory: Eric Fielding and Christopher Milliner; and Sotiris Valkaniotis). We thank Beth Haddon for assistance during field work and production of orthomosaics from UAV photography. Nick Ellett (Lost River Geologic Consulting, LLC) and Zach Engle (U.S. Geological Survey) also contributed to the UAV surveys and orthomosaic production. Bill Hammond, Christine Ruhl, and Jayne Bormann provided helpful insights into the earthquake. Additionally, we thank the cartographic department at NBMG for assistance in map layout and production. Finally, the map sheets and accompanying report were greatly improved through reviews by Steve

Bacon (Desert Research Institute), Rich Briggs (U.S. Geological Survey), and Chris Henry (NBMG).

Support for Dee and Koehler was provided by NBMG. Any use of trade, firm, or product names is for descriptive purposes only and does not imply endorsement by the U.S. Government.

DATA RESOURCES

The geospatial datasets, including a geodatabase and .kmz files are available to download at: http://nbmg.unr.edu/Geohazards/Earthquakes/MonteCristoRangeEQData.html. Earthquake data from the Nevada Seismic Network (UNR, 1971) can be found at the Nevada Seismological Laboratory (NSL) website: http://www.seismo.unr.edu/Earthquake.

REFERENCES

Bacon, S.N., and Pezzopane, S.K., 2007, A 25,000-year record of earthquakes on the Owens Valley fault near Lone Pine, California—implications for recurrence intervals, slip rates, and segmentation models: Geological Society of America Bulletin, v. 119, p. 823–847.

Beanland, S., and Clark, M.M., 1994, The Owens Valley fault zone, eastern California, and surface faulting associated with the 1872 earthquake: U.S. Geological Survey Bulletin 1982, 32 p.

Bell, J.W., dePolo, C.M., Ramelli, A.R., Sarna-Wojcicki, A.M., and Meyer, C.E., 1999, Surface faulting and paleoseismic history of the 1932 Cedar Mountain earthquake area, west-central Nevada, and implications for modern tectonics in the Walker Lane: Geological Society of America Bulletin, v. 111, p. 791–807.

Bennett, R.A., Davis, J.L., and Wernicke, B.P., 1999, Present-day pattern of Cordilleran deformation in the western United States: Geology, v. 27, no. 4, p. 371–374.

Bormann, J., Hammond, W.C., Kreemer, C., and Blewitt, G., 2016, Accommodation of missing shear strain in the central Walker Lane, western North America—constraints from dense GPS measurements: Earth and Planetary Science Letters, v. 440, p. 169–177.

Bormann, J. M, Morton, E.A., Smith, K.D., Kent, G.M., Honjas, W.S., Plank, G.L., and Williams, M.C., 2021, Nevada Seismological Laboratory rapid seismic monitoring deployment and data availability for the 2020 M6.5 Monte Cristo Range, Nevada earthquake sequence: Seismological Research Letters, v. 92, p. 810-822.

Callaghan, E., and Gianella, V.P., 1935, The earthquake of January 30, 1934, at Excelsior Mountains, Nevada: Bulletin of the Seismological Society of America, v. 25, p. 161–168.

DeLano, K., Lee, J., Roper, R., and Calvert, A., 2019, Dextral, normal, and sinistral faulting across the eastern California shear zone-Mina deflection transition, California-Nevada, USA: Geosphere, v. 15, no. 4, p. 1206–1239.

dePolo, C.M., Peppin, W.A., and Johnson, P.A., 1993, Contemporary tectonics, seismicity, and potential earthquake sources in the White Mountains seismic gap, west-central Nevada and east-central California: Tectonophysics, v. 225, p. 271–299.

Dixon, T.H., Miller, M., Farina, F., Wang, H., and Johnson, D., 2000, Present-day motion of the Sierra Nevada block and some tectonic implications for the Basin and Range province, North America Cordillera: Tectonics, v. 19, no. 1, p. 1–24.

Dohrenwend, J.C., 1982, Preliminary surficial geologic map of the Excelsior Mountains area, west-central Nevada: U.S. Geological Survey Miscellaneous Field Studies Map MF-1372, scale 1:62,500.

Elliott, A. J., Dee, S., Koehler, R. D., Barnhart, W. D., Briggs, R., Collett, C., Dawson, T., DeLong, S., Gold, R.D., Haddon, E. K., Hartsorn, E., Hatem, A. E., Milliner, C., Pickering, A. Pierce, I., Seitz, G. G., Trexler, C., Wicks, C., Xu, X., and Zachariasen, J., 2020, Comparison of ground-based and space-based surface rupture mapping of the May 15, 2020 M6.5 Monte Cristo Range earthquake, Nevada: Poster #107 at 2020 SCEC Annual Meeting, SCEC Contribution #10489.

Faulds, J.E., and Henry, C.D., 2008, Tectonic influences on the spatial and temporal evolution of the Walker Lane—an incipient transform fault along the evolving Pacific–North American plate boundary, *in* Spencer, J.E., and Titley, S.R., editors, Ores and orogenesis—circum-Pacific tectonics, geologic evolution, and ore deposits: Arizona Geological Society Digest, v. 22, p. 437–470.

Haddon, E. K., Amos, C.B., Zielke, O., Jayko, A.S., and Burgmann, R., 2016, Surface slip during large Owens Valley earthquakes: Geochemistry, Geophysics, Geosystems, v. 17, p. 2239–2269.

Hammond, W.C., and Thatcher, W., 2007, Crustal deformation across the Sierra Nevada, northern Walker Lane, Basin and Range transition, western United States measured with GPS, 2000–2004: Journal of Geophysical Research-Solid Earth, v. 112, B05411, 26 p.

Hammond, W.C., Blewitt, G., Kreemer, C., Koehler, R.D. and Dee, S., 2020, Geodetic observation of seismic cycles before, during, and after the 2020 Monte Cristo Range earthquake Seismological Research Letters, v. 92, p. 647–662.

Koehler, R.D., Dee, S., Elliott, A., Hatem, A., Pickering, A., Pierce, I., Seitz, G., 2021, Field response and surface rupture characteristics of the 2020 M6.5 Monte Cristo Range earthquake, central Walker Lane, Nevada: Seismological Research Letters, v. 92, p. 823-839.

Lee, J., Hoxey, A.K.R., Calvert, A., Dubyoski, P., 2020, Plate boundary trench retreat and dextral shear drive intracontinental fault-slip histories—Neogene dextral faulting across the Gabbs Valley and Gillis Ranges, Central Walker Lane, Nevada: Geosphere, v. 16, no. 5, p. 1249–1275.

Lifton, Z., Newman, A.V., Frankel, K.L., Johnson, C.W., and Dixon, T.H., 2013, Insights into distributed plate rates across the Walker Lane from GPS geodesy: Geophysical Research Letters, v. 40, p. 4620–4624.

Nagorsen-Rinke, S., Lee, J., and Calvert, A., 2013, Pliocene sinistral slip across the Adobe Hills, eastern California-western Nevada—kinematics of fault slip transfer across the Mina deflection: Geosphere, v. 9, no. 1, p. 37–53.

Oldow, J., Kohler, G., and Donelick, R.A., 1994, Late Cenozoic extensional transfer in the Walker Lane strike-slip belt, Nevada: Geology, v. 22, p. 637–640.

Petronis, M. S., Geissman, J. W., Oldow, J. S., and McIntosh, W. C., 2009, Late Miocene to Pliocene vertical-axis rotation attending development of the Silver Peak-Lone Mountain displacement transfer zone, west-central Nevada *in* Oldow, J.S., and Cashman, P.H., editors, Late Cenozoic structure and evolution of the Great Basin-Sierra Nevada Transition: Geological Society of America Special Paper 447, p. 215–253.

Pierce, I.K.D., Wesnousky, S.G., Owen, L.A., Li, X., Bormann, J.M., and Caffee, M., 2021, Accommodation of plate motion in an incipient strike-slip system—the central Walker Lane: Tectonics, v. 40.

Ruhl, C.J., Morton, E.A., Bormann, J.M., Hatch-Ibarra, R., Ichinose, G., and Smith, K., 2021, Complex fault geometry of the 2020 M_{ww}6.5 Monte Cristo Range, Nevada earthquake sequence: Seismological Research Letters xx.

Ryall, A.S., and Priestly, K., 1975, Seismicity, secular strain, and maximum magnitude in the Excelsior Mountains area, western Nevada and eastern California: Geological Society of America Bulletin, v. 86, p. 1585–1592.

Stewart, J.H., 1988, Tectonics of the Walker Lane belt, western Great Basin—Mesozoic and Cenozoic deformation in a shear zone *in* W.G. Ernst, editor, Metamorphism and crustal evolution of the western United States (Rubey Volume VII): Englewood Cliffs, New Jersey, Prentice-Hall, p. 681–713.

Stewart, J.H., Kelleher, P.C., and Zorich, E.A., 1994, Geologic map of the Monte Cristo Range area, Esmeralda and Mineral counties, Nevada: U.S. Geological Survey Miscellaneous Field Studies Map MF-2260, scale 1:62,500, 15 p.

University of Nevada, Reno (UNR), 1971, Nevada Seismic Network: International Federation of Digital Seismograph Networks, Online, https://doi.org/10.7914/SN/NN.

U.S. Geological Survey (USGS), 2006, Quaternary fault and fold database of the United States: U.S. Geological Survey database, Online, https://earthquake.usgs.gov/hazards/qfaults/, accessed June 2020.

Wesnousky, S.G., 2005, Active faulting in the Walker Lane: Tectonics, v. 24, TC3009, 35 p.

Suggested Citation:

Dee, S., Koehler, R.D., Elliott, A.J., Hatem, A.E., Pickering, A.J., Pierce, I., Seitz, G.G., Collett, C.M., Dawson, T.E., De Masi, C., dePolo, C.M., Hartshorn, E.J., Madugo, C.M., Trexler, C.C., Verdugo, D.M., Wesnousky, S.G., and Zachariasen, J.., 2021, Surface Rupture Map of the 2020 M 6.5 Monte Cristo Range earthquake, Esmeralda and Mineral counties, Nevada: Nevada Bureau of Mines and Geology Map 190, 2 sheets, scale 1:14,000, 26p.

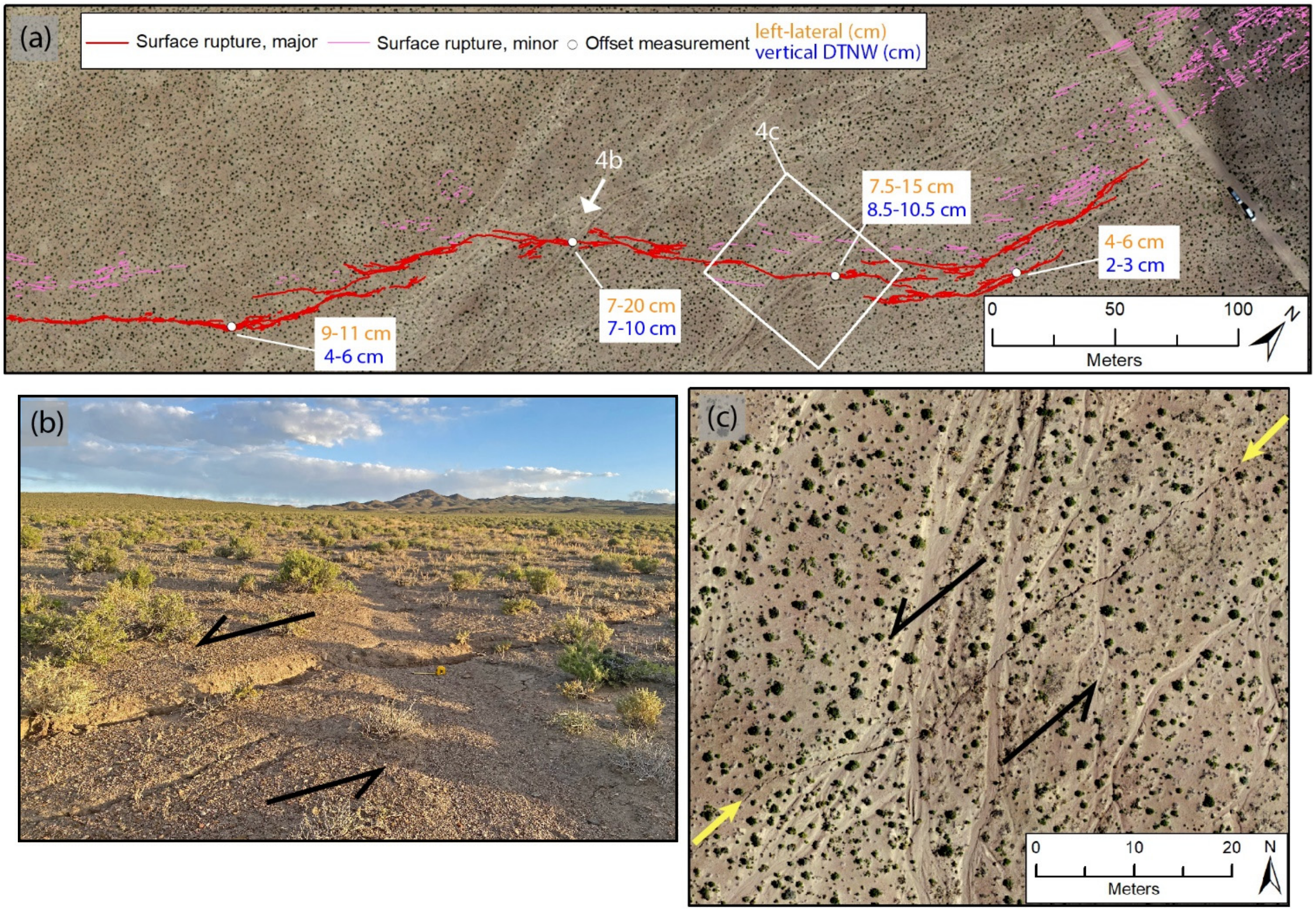

Figure 4. Rupture in the northern main trace of the western domain. Rupture cuts across a low-gradient piedmont slope with no pre-existing scarps or adjacent tectonic geomorphology and offsets Holocene to latest Pleistocene alluvial-fan deposits. The largest left-lateral offsets measured along the entire 2020 surface rupture occur in this area. a) Rupture mapping on orthomosaic showing offset measurements; b) field photo (view to southwest) of oblique left-lateral displacement of a channel margin, with 7–20 cm of left-lateral and 7–10 cm of down-to-the-northwest (DTNW) vertical offset measured at this location; c) orthomosaic of a single consolidated section of rupture in young alluvial sediment.

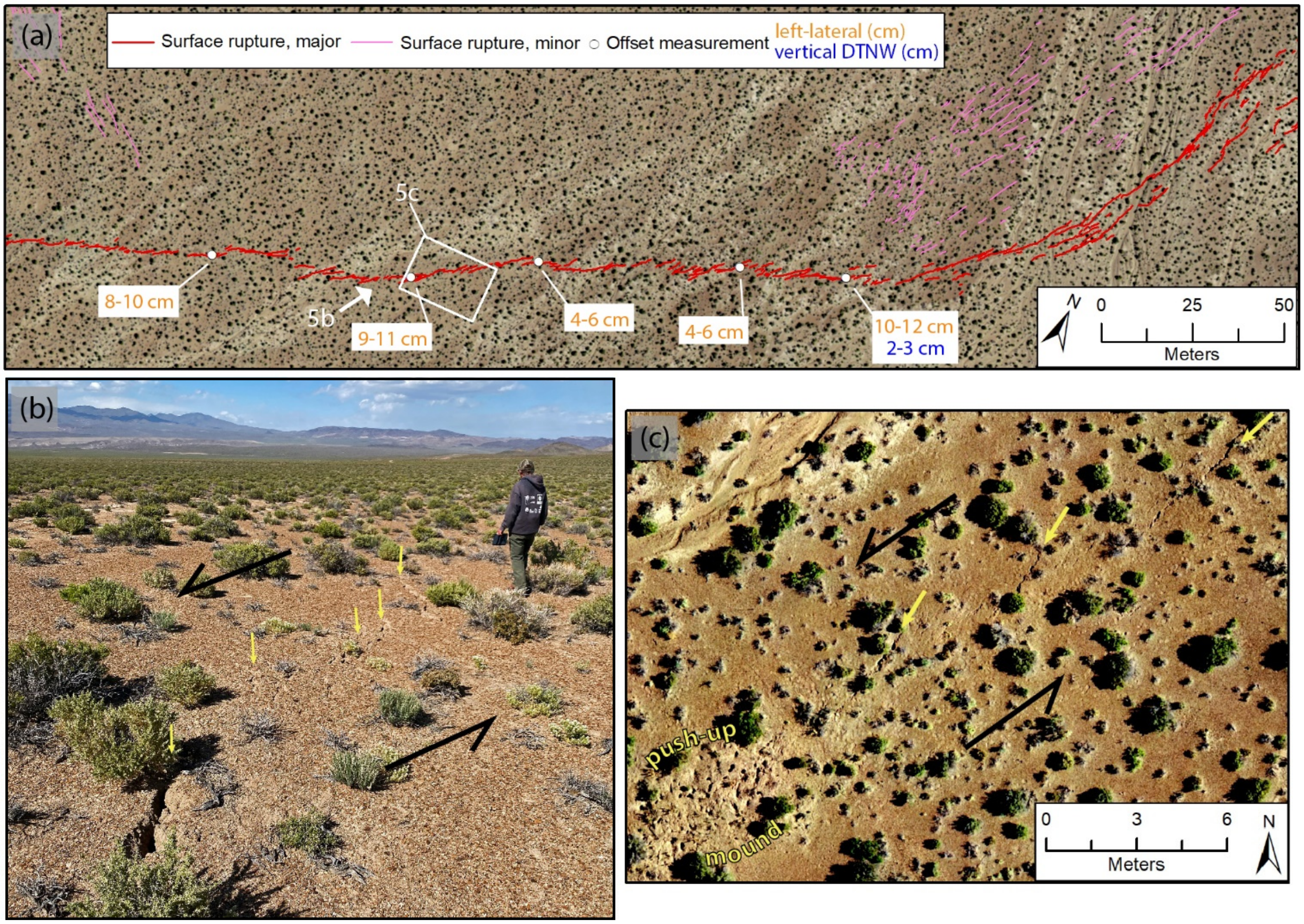

Figure 5. Rupture in the northern main trace, western domain, illustrating left-lateral rupture geometry characterized by a right-stepping en échelon pattern of cracks and push-up mounds. The rupture exhibits a relatively narrow zone of deformation that crosses Holocene to late Pleistocene alluvial-fan deposits with no evidence of prior faulting. a) Rupture mapping on orthomosaic showing the location of offset measurements; b) field photo (view to northeast) of right-stepping en échelon surface ruptures in left laterally offset alluvium; c) orthomosaic of right-stepping en échelon ruptures and a compressional push-up mound.

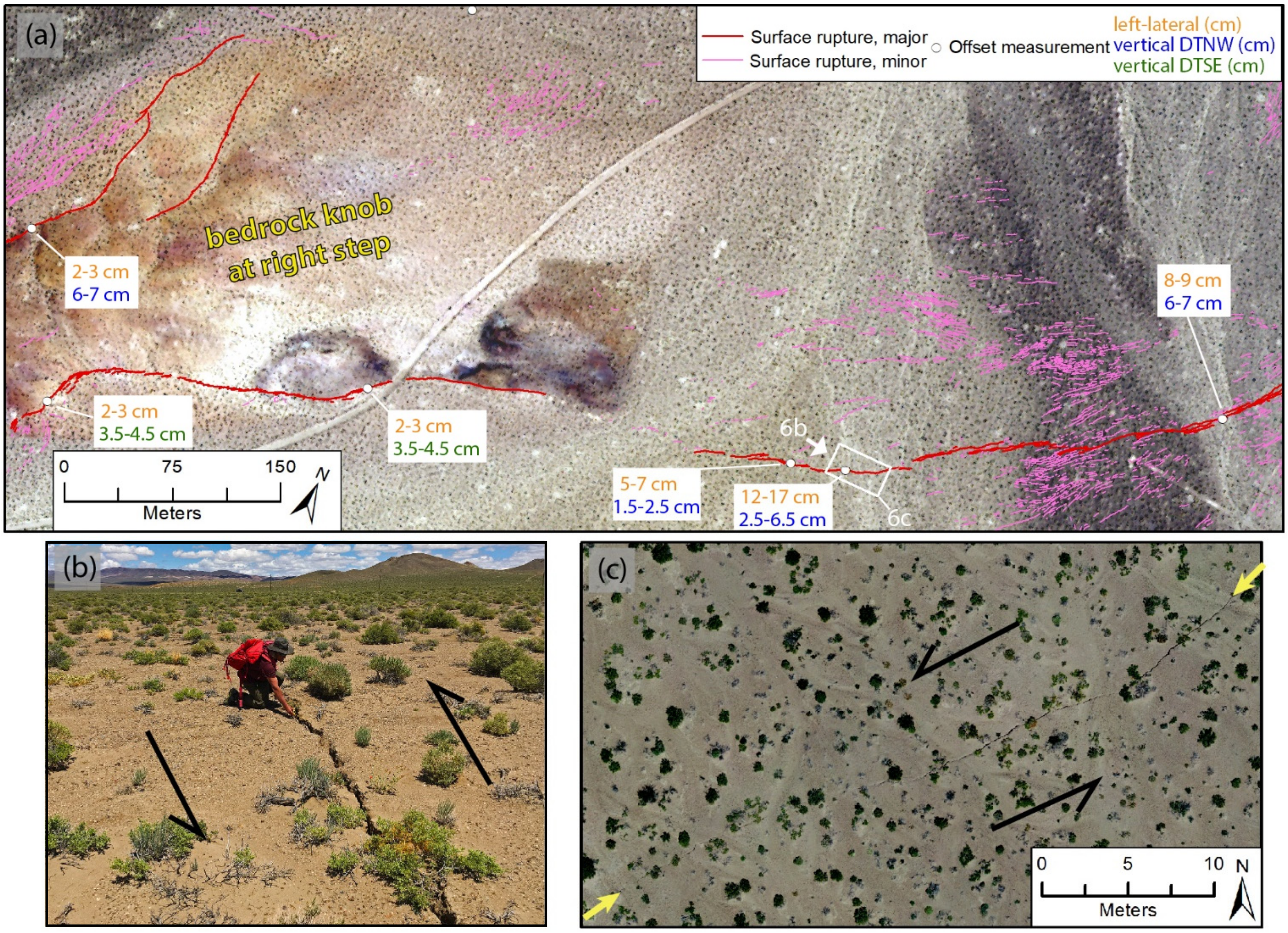

Figure 6. Rupture in the northern main trace, western domain, illustrating faulted alluvial deposits and local alignment of surface ruptures with geomorphic features suggesting progressive deformation in the area. Here, a left-oblique down-to-the-northwest (DTNW) rupture steps right across a topographically elevated bedrock knob to a left-oblique down-to-the-southeast (DTSE) rupture. The bedrock knob is 2 m higher in elevation than the surrounding alluvium suggesting prior rupture(s) at this location. a) Rupture mapping on satellite imagery showing the location of offset measurements and the location of the right step at a fault-bounded bedrock knob; b) field photo (view to southeast) of oblique left-lateral offset of active alluvial channels, with 12–17 cm of left-lateral and 2.5–6.5 cm of down-to-the-northwest vertical displacement measured at this location; c) orthomosaic of a linear section of rupture in young alluvial sediment. Rupture extends between yellow arrows.

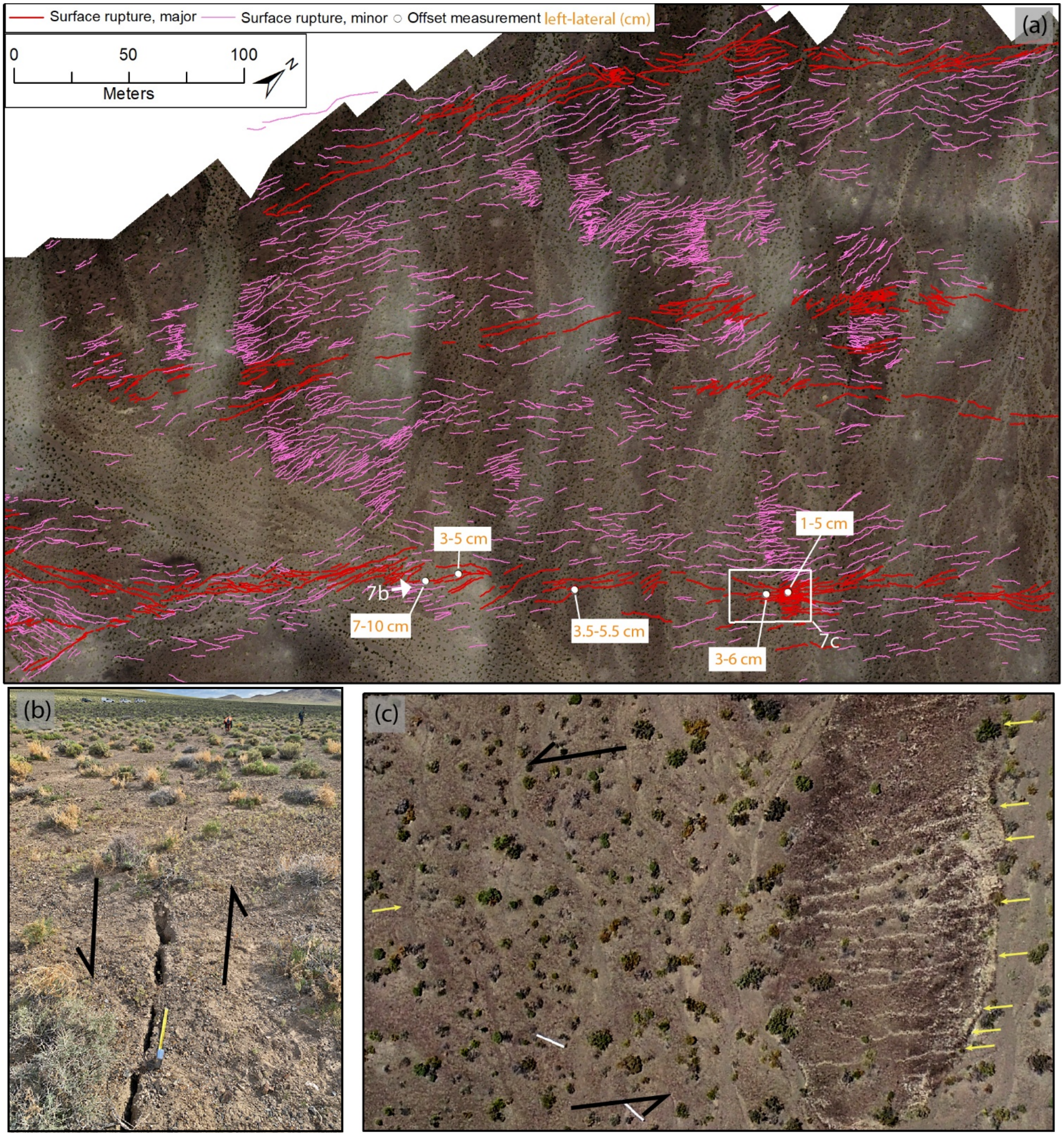

Figure 7. Rupture in the southern main trace of the western domain. The ruptures in this area are characterized by exceptionally distributed deformation spread over an 800-m-wide-zone of closely spaced cracks in alluvial-fan deposits. a) Rupture mapping on orthomosaic and location of offset measurements; b) field photo (view to east) of one of the more prominent ruptures; c) orthomosaic showing well-defined and closely spaced ruptures across a relatively older alluvial-fan surface (yellow arrows).

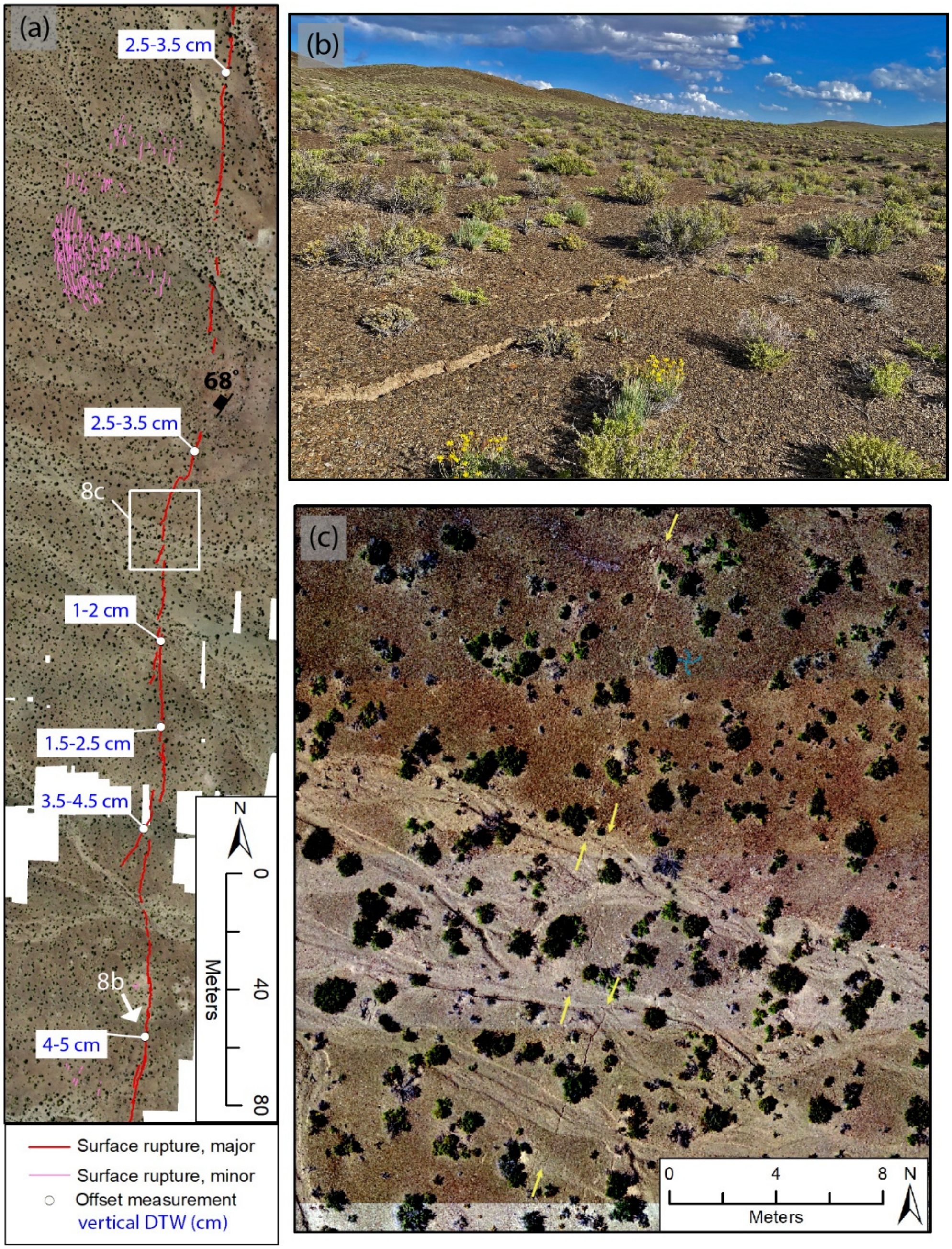

Figure 8. North-striking rupture, western domain, illustrating down-to-the west (DTW) vertical offset in alluvial-fan deposits along the western base of bedrock hills. a) Rupture mapping on orthomosaic showing location of offset measurements and the orientation of an exposed bedrock fault surface located on-strike with the surface rupture (fault surface=217°/68°); b) field photo (view to southeast) of vertically offset (4–5 cm, down-to-the-west) alluvium with well-developed desert pavement; c) orthomosaic of rupture cutting variously aged alluvial deposits including unconsolidated sediment in active channels (lighter colors) and older fan gravels with desert pavement (darker colors).

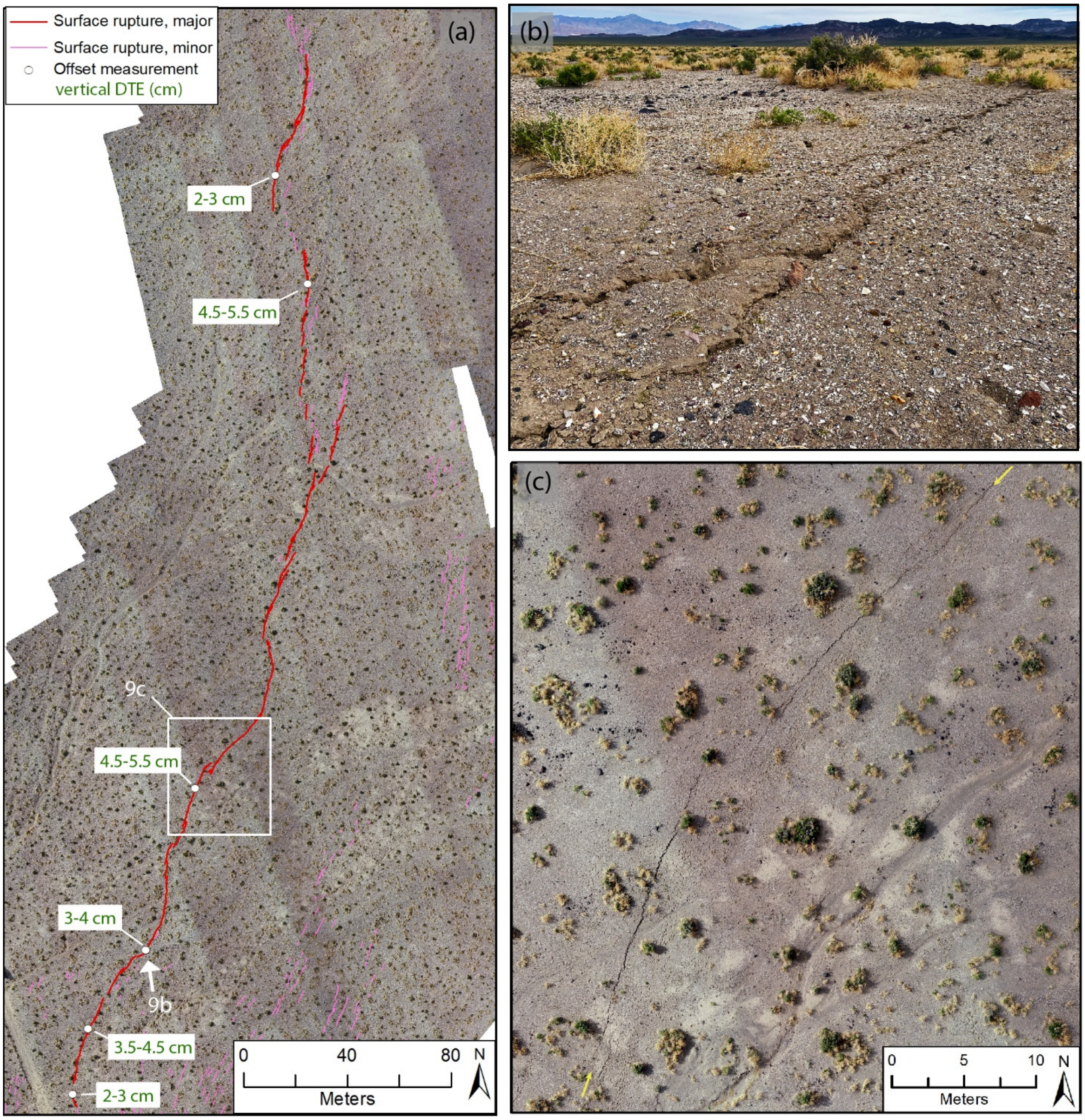

Figure 9. Typical extensional deformation along a north-striking rupture in the eastern domain. a) Rupture mapping on orthomosaic showing location of offset measurements; b) field photo (view to northwest) of down-to-the-east (DTE) vertical separation (2–5 cm) of Holocene alluvium; c) orthomosaic of a linear section of rupture in Holocene alluvium.

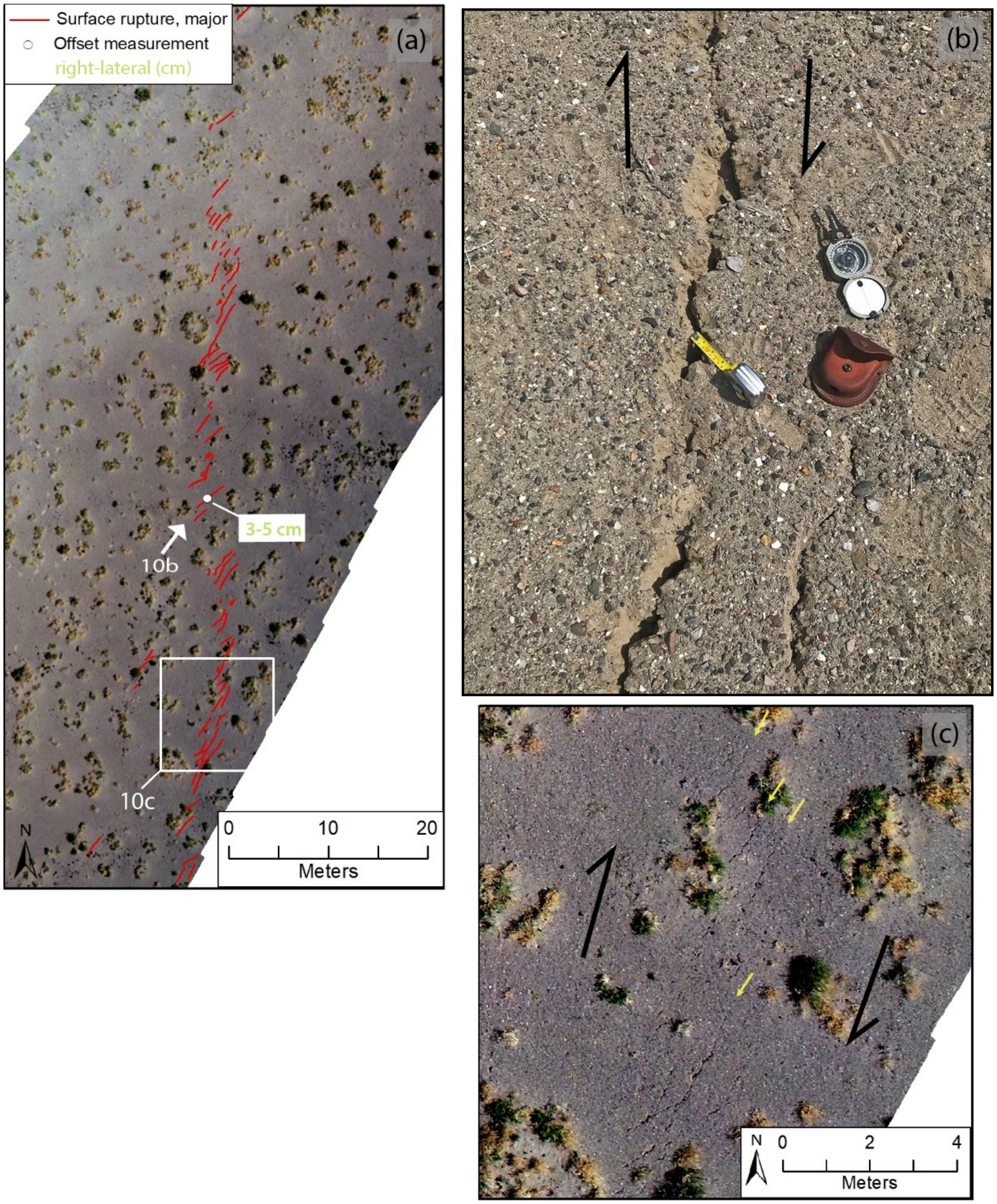

Figure 10. North-striking rupture in the eastern domain with right-lateral slip. a) Rupture mapping on orthomosaic showing location of measured right lateral offset and left-stepping en échelon cracks along a north-northeast trending rupture; b) field photo (view to northeast) of 3–5 cm of right-lateral offset of alluvium, Brunton compass has a north orientation; c) orthomosaic of left-stepping en échelon ruptures that are characteristic of right-lateral slip.

Table 1. Field offset measurements from the 2020 M6.5 Monte Cristo Range earthquake

Lateral Offset (cm)	Lateral Sense	Vertical Offset (cm)	Vertical Sense	Rupture Azimuth (˚)	Date	Author	Notes	Latitude	Longitude
1–3	LL	1–3	DTNW	030	5/17/2020	Pickering	2 cm LL, 2 cm down to northwest	38.09906	-118.09658
-	-	1–3	DTNW	031	5/17/2020	Pickering	Matching crack edge, opening accommodating left-lateral shear. Mapping along pre-existing scarp approximately 50 cm high. Opening of 4 cm, with 2 cm down to northwest	38.09922	-118.09644
1–3	LL	-	-	060	5/17/2020	Hatem	Opening ~ 2 cm with apparent LL, oriented ~ 060?	38.09934	-118.09626
-	-	3	DTNW	055	5/18/2020	Dee	Rupture at base of 0.5 m paleoscarp, 3 cm offset, scarp is in Holocene fan deposits	38.09954	-118.09607
-	-	2.5	DTNW	040	5/18/2020	Dee	Rupture, 2.5 cm down to NW offset	38.10054	-118.09485
0.5–1.5	LL	-	-	040	5/26/2020	Hatem	060 opening direction with ~1 cm apparent left-lateral opening, crack striking ~ 040	38.10055	-118.09483
1–2	LL	-	-	075	5/18/2020	Pickering	3–4 strands, 5–10 width. One strand shows 2 cm apparent left lateral	38.10332	-118.09241
-	-	1–3	DTE	000	5/26/2020	Hatem	Enigmatic stepover, potentially left lateral	38.13047	-118.05585
-	-	3–5	DTE	000	5/26/2020	Hatem	Fault strike 000, steps right into releasing with ~4 cm down to the east, then steps back to the east with ~4 cm of diffuse uplift/warping across restraining bend	38.13077	-118.05585
-	-	3–4	DTE	000	5/26/2020	Pickering	Continuing 000, down to the east 3–4 cm	38.13107	-118.05585
3–5	RL	-	-	032	5/26/2020	Pickering	Strike 032. 4 cm opening, 4 cm right lateral on western channel edge. Fault runs parallel to channel	38.13253	-118.05591
9–11	LL	-	-	045	5/26/2020	Hatem	Crack system striking 045. Left lateral vector 040, with apparent displacement of 10 cm +/- 1 cm.	38.13265	-118.05584
-	-	3–4	DTE	005	5/16/2020	Dee	Largest crack in this zone, vertical offset, up to 3–4 cm vertical north side up	38.14357	-117.93453
-	-	3	DTE	000	5/16/2020	Dee	Likely NE most crack here, zone appears to be isolated, 2 cm down to south, one cobble looks to be rotated clockwise	38.14441	-117.93461
-	-	2	DTE	000	5/16/2020	Dee	Main NS rupture continues, ~2 cm down to east	38.14850	-117.95620

Table 1. Field offset measurements from the 2020 M6.5 Monte Cristo Range earthquake

Lateral Offset (cm)	Lateral Sense	Vertical Offset (cm)	Vertical Sense	Rupture Azimuth (˚)	Date	Author	Notes	Latitude	Longitude
-	-	2–3	DTE	350	5/16/2020	Dee	Rupture continues 2–3 cm down to east vertical	38.14912	-117.93756
-	-	4	DTE	025	5/16/2020	Dee	Rupture continues, 4 cm vertical	38.14935	-117.93750
-	-	3–4	DTE	030	5/16/2020	Dee	Fracture continues down to east 3–4 cm	38.14962	-117.93725
-	-	3–4	DTE	010	5/16/2020	Dee	Rupture 3–4 cm vertical	38.14992	-117.93716
-	-	5	DTE	025	5/16/2020	Dee	Rupture 5 cm down to east vertical	38.15018	-117.93704
-	-	5	DTE	340	5/16/2020	Dee	5 cm down to east	38.15194	-117.93657
-	-	3–5	DTE	015	5/16/2020	Dee / Koehler	Rupture continues, 5 cm vertical	38.15232	-117.93672
10		7	DTN	080	5/22/2020	Seitz / Koehler	10 cm LL, 7 cm vertical up on S, 80 deg, but bends to N abruptly	38.15366	-118.03688
-	-	0.5–3	DTE	020	5/22/2020	Seitz		38.15468	-118.03291
-	-	1–3	DTE	005	5/22/2020	Seitz		38.15520	-118.03247
2–4 LL	LL	-	-	065	5/16/2020	Koehler		38.15742	-117.88003
3–5	RL	-	-	029	5/17/2020	Pickering	Following lineament. Fault left-stepping en échelon. N29E overall trend. 4 cm slip vector, 145 slip vector azimuth. Right lateral. Possibly 1 cm of vertical locally. Not at this measurement site though	38.16105	-117.91923
1	LL	-	-	045	5/22/2020	Seitz		38.16249	-118.02213
3–4	RL	-	-	030	5/17/2020	Pickering	Left-stepping en échelon. N30E slip vector, 3.75 cm (minimum 3 cm , maximum 4 cm), N30E slip vector ~1 cm. Crack edge offset. Sites showing slip are no more than 3 m in length. Continuous cracks are small, en échelon and lack discernible measurement.	38.16290	-117.91920
1–3	LL	-	-	025	6/4/2020	Hatem	Crack strikes 025 opening left directed 080 opening 2 cm vague measurement due to semi degraded crack	38.16428	-118.01474
2.5–3.5	LL	2	DTNW	035	5/18/2020	Dee	Very good fracture with ~3 cm left lateral, down to the west 2 cm	38.16539	-118.01862
1–2	RL	-	-	035	5/17/2020	Pickering	3 cm tension. 1 cm RL. 035	38.16614	-117.91898

Table 1. Field offset measurements from the 2020 M6.5 Monte Cristo Range earthquake

Lateral Offset (cm)	Lateral Sense	Vertical Offset (cm)	Vertical Sense	Rupture Azimuth (˚)	Date	Author	Notes	Latitude	Longitude
-	-	1–3	DTNW	030	6/4/2020	Hatem	030 striking cracks with NW side down ~2 cm	38.16641	-118.01061
1–3	RL	2–3	DTW	005	6/4/2020	Hatem	Opening with implied right lateral based on opening and closing along variability in strike. Very degraded. Strike 005	38.16703	-118.00592
-	-	3–5	DTW	015	6/4/2020	Pickering	Localized large crack, cuts into base of hillside. Strike 015. Locally down to the west 3–5 cm. Opening 3–4 cm. Depth of crack 20 cm	38.16776	-118.00429
10	LL	4–6	DTNW	050	5/22/2020	Dee	~10 cm LL, 2–3 tightly packed ruptures, 4–6 cm vertical down north, good site for detail	38.16829	-118.03833
9–11	RL	-	-	355	5/17/2020	Pickering	Location of good first 10 cm offset. Detailed measurements. Beginning of fault zone getting bigger	38.16859	-117.91907
7–20	LL	-	-	035	5/22/2020	Seitz	Offset channel measured in detail by Gordon Seitz	38.16934	-118.03738
7.5–15	LL	8.5–10.5	DTNW	035	5/22/2020	Seitz	Offset channel measured in detail by Gordon Seitz	38.16987	-118.03636
7–8	LL	3	DTNW	040	5/21/2020	Dee	-8 cm LL possible very collapsed, 3 cm vertical	38.16991	-118.03630
		5–6	DTNW	055	5/21/2020	Dee	Rupture, vertical continues at 5–6. LL looks to be getting larger	38.17003	-118.03599
5	LL	2–3	DTNW	030	5/21/2020	Dee	Vertical is all down to NW. ~5 cm vertical with 3.5 and 1.5 on each of two strands, nearby spot with most vertical on one strand has 5 cm, 2–3 cm LL measured on a sawtooth	38.17031	-118.03573
-	-	3	DTW	000	5/18/2020	Dee	2–3 strands here easternmost has 3 cm down to west	38.17158	-118.01740
-	-	1	DTW	015	5/21/2020	Dee	Rupture, push-ups and locally 1 cm down to west	38.17174	-118.03005
-	-	2–3	DTW	030	5/18/2020	Dee	Smaller 2–3 cm offset	38.17211	-118.01725
2	RL	4	DTW	015	5/18/2020	Dee	Best surface offset in this zone single strand displaced 4 cm vertically, 2 cm right lateral	38.17252	-118.01713
1–3	RL	5	DTW	005	5/18/2020	Dee	5 cm max vertical offset, 3–4 cm common, 1–3 right lateral	38.17258	-118.01713

Table 1. Field offset measurements from the 2020 M6.5 Monte Cristo Range earthquake

Lateral Offset (cm)	Lateral Sense	Vertical Offset (cm)	Vertical Sense	Rupture Azimuth (˚)	Date	Author	Notes	Latitude	Longitude
8–10	LL	-	-	055	5/19/2020	Koehler	Left-lateral 8–10 cm	38.17305	-118.02355
9–11	LL	-	-	045	5/19/2020	Pickering	10 +/- 1 cm left lateral. Vector azimuth 065. Fault azimuth 045. Crack at this location with depth of 59 cm.	38.17321	-118.02296
-	-	4	DTW	030	5/18/2020	Dee	Single strand here, 4 cm vertical	38.17322	-118.01714
9–11	LL	-	-	045	5/19/2020	Hatem	Opening 10 cm +/- 1 cm, fault orientation 045. To the east the strike is more like 080. Slip vector 65–70	38.17331	-118.02277
4–6	LL	-	-	065	5/19/2020	Pickering	Fault strike 065, crack edge matching, slip vector 5 +/- 1 cm left lateral at 065. Small mounds of compression on either side of measurement location. Fault width 10 m, measurement aperture 10 cm	38.17338	-118.02262
-	-	2	DTW	025	5/18/2020	Dee	Slip reduces here to 2cm vertical	38.17354	-118.01708
4–6	LL	-	-	065	5/19/2020	Hatem	Strike 065. Opening azimuth 060–063. Slip vector 5 +/- 1 cm, left lateral, slip vector 065. Small mounds of compression on either side of measurement location. Fault width 10 m, measurement aperture 10 cm	38.17358	-118.02205
3–5	LL	-	-	039	6/4/2020	Pickering	039 local strike. 4 cm left-lateral crack edge match. Slip vector azimuth 075. N strand over (2 m) shows 6 cm of opening, no lateral	38.17358	-117.99109
5	LL	-	-	035	5/25/2020	Seitz		38.17359	-118.02204
8	LL	-	-	050	5/19/2020	Hatem	Fault orientation 050, slip vector azimuth 90, left-lateral slip vector length 8cm. 8 +/-2 opening. Fault zone width 20 m, several strands	38.17366	-118.02175
11	LL	2.5	DTNW	035	5/25/2020	Seitz	Separation direction 267, 11 cm horizontal, 2.5 cm down to north	38.17367	-118.02174
-	-	4–10	DTE	005	6/4/2020	Hatem	7 plus or minus 3 cm of vertical down to the east. Coarse measurement	38.17370	-117.99091

Table 1. Field offset measurements from the 2020 M6.5 Monte Cristo Range earthquake

Lateral Offset (cm)	Lateral Sense	Vertical Offset (cm)	Vertical Sense	Rupture Azimuth (˚)	Date	Author	Notes	Latitude	Longitude
-	-	1–2	DTW	005	5/18/2020	Dee	2 traces, 1–2 cm slip on east trace	38.17381	-118.01709
-	-	3	DTW	005	5/18/2020	Dee	Fan with well-developed pavement, slip up to 3 cm, hint of right lateral in rotated boulder	38.17440	-118.01696
-	-	2.5–3.5	DTNW	010	5/18/2020	Dee	Continues single strand 3 cm down to west	38.17558	-118.01686
-	-	1–2	DTNW	030	5/19/2020	Dee	Rupture 1–2 cm down to west	38.17603	-118.01669
7–10	LL	-	-	030	6/3/2020	Hatem	Max 10 cm left-lateral opening on 030 crack opening oriented 075	38.17634	-117.98692
3–5	LL	-	-	026	6/3/2020	Pickering	Fault enlarging. Crack with depth of 45 cm. Minimum 5 cm opening. In a zone of cracks approximately 10–20 meters wide	38.17646	-117.98684
		3–4	DTW	010	5/19/2020	Dee	Rupture continues into old fan with 3–4 cm down to west	38.17648	-118.01636
3.5–5.5	LL	-	-	030	6/4/2020	Pickering	Right-stepping, left-lateral single-strand fault. Crack edge matching slip vector length 4.5 cm. Slip vector azimuth 075.	38.17677	-117.98641
3–6	LL	-	-	040	6/4/2020	Pickering	Faulting gone since last point. Reappears here as densely spaced fractures 1–2 m apart. Counted a minimum of 23 strands. Opening vector 83, LL 3 cm +/3 cm (3 is minimum) on single strand. Characterizing zone with geo7x	38.17734	-117.98579
1–5	LL	-	-	030	6/3/2020	Hatem	Deformation is concentrated to a very rigid block. crack with apparent left lateral but very tough to measure. 3 cm +/- 2 cm left lateral directed 083 on a 030 trending crack	38.17741	-117.98573
-	-	1–3	DTNW	050	5/19/2020	Pickering	Rupture cuts obliquely across dirt road, fault changes strike from 030–050. Single strand, continues into desert pavement on either side of dirt road. Tracing with geo7x. Continues onto pre-existing scarp. 2 cm opening, 2 cm v	38.17803	-118.01671
1–2	LL	-	-	050	5/18/2020	Hatem	Bedrock fault in exploration trench, NE trending correct orientation for active faulting, didn't find good slicks	38.17821	-118.01650

Table 1. Field offset measurements from the 2020 M6.5 Monte Cristo Range earthquake

Lateral Offset (cm)	Lateral Sense	Vertical Offset (cm)	Vertical Sense	Rupture Azimuth (˚)	Date	Author	Notes	Latitude	Longitude
2	LL	-	-	040	5/19/2020	Pickering	Fault rupture intersects desert pavement, tightens up and shows nicely. 2 cm LL slip vector, 075–080 slip vector azimuth, fault strike 040	38.17837	-118.01610
1–3	LL	-	-	030	6/3/2020	Hatem	Solid crack with 2–3 cm opening LL. Crack strikes 030, opening 080. One main fault with subsidiary strands ~2 m to the south (left stepping)	38.17858	-117.98305
2–3	LL	4	DTE	005	5/19/2020	Dee	Measured 4 cm vertical 2–3 cm LL	38.18107	-118.01268
2–4	LL	-	-	025	6/2/2020	Hatem	Crack striking 025. The opening is degraded and caving, minimum of 3 cm left-lateral displacement oriented in the 075 opening direction. Feature is relatively poor for measurement	38.18117	-117.96561
-	-	1–3	DTNW	020	6/3/2020	Hatem	Still on 020 oriented crack. North side down with ~2 cm vertical separation. Very degraded	38.18137	-118.01390
1–3	LL	-	-	030	6/2/2020	Hatem	Fault zone ~10 m wide. One main strand with short (<1 m cracks) all around. Main fault zone strikes 030. LL opening 2 cm directed 075. ~23 cm deep crack here	38.18143	-117.96515
-	-	1–3	DTSE	025	6/3/2020	Hatem	Crack striking 040–045. ~2 cm down to the south vertical separation	38.18192	-117.97666
2–3	LL	6–7	DTNW	030	5/19/2020	Dee	Faulted young micro fan with measurable offset, 6–7 cm vertical, 2–3 cm of left lateral based on displaced rupture edges and circular root zones, and tiny gully risers. Rupture is at a likely preexisting scarp	38.18200	-118.01338
2–3	LL	3.5–4	DTSE	035	5/19/2020	Dee	Very nice down to SE LL rupture, 3.5 to 4 cm down, 2 to 3 cm LL two measurements	38.18201	-118.01044
2–3	LL	-	-	070	6/3/2020	Hatem	LL apparent opening in direction of 095. 2.5 cm +/- 0.5 cm crack orientation 070	38.18241	-117.97554

Table 1. Field offset measurements from the 2020 M6.5 Monte Cristo Range earthquake

Lateral Offset (cm)	Lateral Sense	Vertical Offset (cm)	Vertical Sense	Rupture Azimuth (˚)	Date	Author	Notes	Latitude	Longitude
5–7	LL	2	DTNW	070	5/19/2020	Dee	Strand continues, looks to be a major rupture, measured 5–7 cm LL, 2 cm vertical down to NW	38.18273	-118.00717
6	LL	3	DTNW	085	5/19/2020	Dee	Displaced channel margin LL 6 cm measured from jigsaw part of fracture (not channel margin which was fuzzy), 3 cm vertical down to NW	38.18276	-118.00695
4	LL	3	DTNW	065	5/20/2020	Dee	4 cm LL / 3 cm vertical	38.18281	-118.00683
12.5–17.5	LL	2.5–4.5	DTNW	070	5/21/2020	Seitz	Detail offset measurement by Gordon Seitz	38.18282	-118.00679
12–17	LL	4–6.5	DTNW	065	5/23/2020	Seitz	Detailed offset measurement by Gordon Seitz	38.18283	-118.00675
1–3	LL	-	-	010	6/3/2020	Hatem	2 cm LL offset (very degraded) slip vector = 065. Crack strikes 010. Slope parallel—could be gravitational/shaking related. Within moderately well developed pavement with angular cobbles on top of softer alluvium	38.18288	-117.97498
11–16	LL	4.5–6.5	DTNW	073	5/23/2020	Seitz	Detail offset measurement by Gordon Seitz	38.18289	-118.00656
6–7	LL	5.5–6	DTNW	035	5/20/2020	Dee	Rupture with measurable offset. 6–7 cm measured on sawtooth, 5.5–6 cm vertical	38.18293	-118.00649
8–9	LL	8–9	DTNW	050	5/19/2020	Dee	Rupture. 8–9 cm minimum vertical, down to northwest. ~8–9 cm LL, area got saturated by rain	38.18390	-118.00467
8–9	LL	6–7	DTNW	075	5/20/2020	Dee	Another spot with ok offset measurement. 8–9 LL, 6–7 vertical	38.18396	-118.00451
3–4	LL	4	DTNW	050	5/20/2020	Dee	Channel margins are displaced LL and DTNW. NW strand has ~8–9 cm LL on channel margin, 6–7 cm vertical, SE strand 3–4 cm LL on sawtooth pieces	38.18405	-118.00432
8–9	LL	6–7	DTNW	050	5/20/2020	Dee	Another left deflected channel margin	38.18415	-118.00424
-	-	4	DTSE	030	5/19/2020	Dee	Rupture with 4 cm down to SE, NE striking	38.18442	-118.01099
-	-	2–3	DTNW	040	5/20/2020	Dee	Rupture in old fan, 2–3 cm down to NW, ambiguous lateral	38.18477	-118.00290

Table 1. Field offset measurements from the 2020 M6.5 Monte Cristo Range earthquake

Lateral Offset (cm)	Lateral Sense	Vertical Offset (cm)	Vertical Sense	Rupture Azimuth (˚)	Date	Author	Notes	Latitude	Longitude
-	-	2	DTNW	025	5/20/2020	Dee	ENE rupture with measurable offset. 2 cm down to west, measured 2 cm right lateral on a strand	38.18592	-118.00238
2–3	LL	2	DTNW	050	5/20/2020	Dee	ENE ruptures with measurable LL and DTNW offset, 2 cm vertical, 2–3 cm LL	38.18615	-118.00052
1–3	LL	1.5	DTNW	013	5/20/2020	Dee	Rupture, oriented ENE, 1.5 cm vertical down to NW, ~1–3 cm LL	38.18744	-117.99992
-	-	2	DTW	000	5/20/2020	Dee	N-S rupture with up to 2 cm down to west	38.18798	-118.00066
-	-	2	DTNW	030	5/20/2020	Dee	Rupture, parallels bedrock contact, ENE, 2 cm DTNW	38.18943	-117.99975
-	-	4	DTNW	035	5/20/2020	Dee	Breaks into a couple strands, lots of fissuring ruptures 4 cm DTNW vertical across both strands. Rain saturated material so no lateral measurement	38.19057	-117.99873
-	-	1	DTE	015	5/21/2020	Dee	Slight down to east maybe 1 cm	38.19158	-118.01336
-	-	4	DTSE	020	5/20/2020	Dee	NE-trending rupture zone in old fan 3–4 strands one with 4 cm max down to SE, no lateral seen	38.19181	-117.99623
2	LL	-	-	065	5/20/2020	Dee	East-west rupture crosses road, 2 cm of left lateral measured on sawtooth	38.19247	-118.00098
3	LL	-	-	070	5/20/2020	Seitz		38.19251	-118.00087
-	-	1–2	DTSE	062	5/21/2020	Dee	SE most rupture, sawtooth, 1–2 cm down to SE continues 4 m to NE, 10 cm to SW	38.19313	-117.99616
4	RL	-	-	054	5/20/2020	Dee	ESE rupture with 4 cm measured RL offset. Complex zone with short fractures in other orientations	38.19326	-118.00127
-	-	2–3	DTNW	054	5/20/2020	Dee	NE-trending rupture with approximate 2–3 cm down to NW rupture	38.19334	-118.00038
1	LL	1–3	DTSE	040	5/18/2020	Seitz	1 cm LL, 1cm vert, up to max 3 cm vert	38.19771	-118.05125

Table 1. Field offset measurements from the 2020 M6.5 Monte Cristo Range earthquake

Lateral Offset (cm)	Lateral Sense	Vertical Offset (cm)	Vertical Sense	Rupture Azimuth (˚)	Date	Author	Notes	Latitude	Longitude
-	-	2–4	DTNW	002	6/5/2020	Pickering	3 cm vertical, down to the west, (left stepping but no measurable lateral). Local strike 002, overall zone 026	38.24584	-117.82867
-	-	3–5	DTNW	018	6/5/2020	Pickering	Strike 018. Here vertical separation 4 cm, opening 2 cm. 2 m to south, vertical 0.5 and opening 3.5 +/- 0.5 cm, opening azimuth 105. Along paleoscarp	38.24646	-117.82821
-	-	3–5	DTNW	018	6/5/2020	Pickering	Local strike 018. 4 cm DTNW, fault obliquely cutting wash	38.24664	-117.82815
-	-	2–4	DTNW	020	6/5/2020	Pickering	Strike 020. Local down to the west vertical separation, 3 cm. Nothing to measure lateral	38.24674	-117.82811
1–3	LL	-	-	020	6/5/2020	Hatem	Fault, slight left lateral (potential) = 2 cm +/- 1 cm. slip vector = 070; crack strikes 020	38.25421	-117.82970
0.5–3	RL	-	-	005	6/5/2020	Hatem	~1 cm RL opening (hard to measure/relative) oriented 310 on crack striking 005 and right lateral opening ~1–2 cm oriented 315. Crack orientation = 005	38.26307	-117.83496

Notes: DTNW = down-to-the-northwest, DTN = down-to-the-north, DTSE = down-to-the-southeast, DTE = down-to-the-east, DTW = down-to-the-west, LL = left-lateral, RL = right-lateral

Table 2. Summary of rupture map features shown on Sheets 1 and 2 and accompanying geospatial dataset

Map Feature	Definition	Summary of fields in geospatial database	
Surface rupture, major and Surface rupture, minor*	Surface rupture, major = linear, relatively continuous cracks or fractures with locally measurable offset of surficial deposits or geomorphic features Surface rupture, minor = relatively discontinuous cracks or fractures (<1 to 10s of meters long) with offsets too small to be reliably measured (<~1 cm)	"Author"	Name of author that collected the GPS line or digitized the line on a UAV orthophoto
		"Source"	Source of data: *Garmin GPS line, Geo7x line, ipad GPS line, iphone GPS line* = traces walked with GPS units recording tracks ipad GPS pts = traces interpolated between GPS points *UNR_UAV, USGS_UAV* = traces drawn on UAV orthophotomosaics
Offset measurement	Amount and sense of coseismic surface offset (cm)	"Notes"	Field notes
		"lateral_cm"	Lateral offset measurement (cm)
		"lat_sense"	Sense of lateral offset (*LL*=left-lateral, *RL*=right-lateral)
		"vertical_cm"	Vertical offset measurement (cm)
		"vert_sense"	Sense of vertical offset (*DTNW* = down-to-the-northwest, *DTN* = down-to-the-north, *DTSE* = down-to-the-southeast, *DTE* = down-to-the-east, *DTW* = down-to-the-west)
		"Author"	Name of author that collected the measurement
		"Display"	Displayed on sheets 1 or 2, some measurements omitted for clarity but kept in geodatabase (*Y*=yes, *N*= no)
Rupture orientation	Azimuth orientation of rupture; only displayed on the map in areas with no mapped rupture trace	"Notes"	Field notes
		"Author"	Name of author that collected the measurement
		"Attitude"	Azimuth of rupture
		"Display"	Displayed on sheets 1 or 2, many measurements omitted for clarity but kept in geodatabase (*Y*=yes, *N*= no)
Distributed ruptures	Zones of distributed coseismic ruptures but lacking detailed rupture mapping or UAV orthomosaics		
Extent of post-event UAV orthomosaics	Spatial extent of low altitude aerial imagery (orthomosaic) coverage using Uncrewed Aerial Vehicles	"GCP"	Ground control points used for orthomosaics production (*Y*=yes, *N*= no)
		"Notes"	Notes on contributor that flew the UAV data acquisition

Notes: *The geospatial datasets include additional line observations not shown on sheets 1 and 2 such as "ambiguous" traces defined as linear features with low confidence in coseismic origin, and "secondary" defined as features confidently inferred to have been produced by ground-shaking effects rather than tectonic deformation (e.g., mass wasting, liquefaction).